Altiratinib blocks Toxoplasma gondii and Plasmodium falciparum development by selectively targeting a spliceosome kinase

Christopher Swale, Valeria Bellini, Matthew Bowler, Nardella Flore, Marie-Pierre Brenier-Pinchart, Dominique Cannella, Lucid Belmudes, Caroline Mas, Yohann Couté, Fabrice Laurent, et al.

Altiratinib blocks *Toxoplasma gondii* and *Plasmodium falciparum* development by selectively targeting a spliceosome kinase

Christopher Swale[1†*], Valeria Bellini[1†], Matthew W. Bowler[2], Nardella Flore[3], Marie-Pierre Brenier-Pinchart[1], Dominique Cannella[1], Lucid Belmudes[4], Caroline Mas[5], Yohann Couté[4], Fabrice Laurent[6], Artur Scherf[3], Alexandre Bougdour[1*] and Mohamed-Ali Hakimi[1 *]

[1] Institute for Advanced Biosciences (IAB), Team Host-pathogen interactions and immunity to infection, INSERM U1209, CNRS UMR5309, University Grenoble Alpes, Grenoble, France

[2] European Molecular Biology Laboratory, Grenoble, 71 Avenue des Martyrs, CS 90181, 38042 Grenoble, France.

[3] Institut Pasteur, Université de Paris, Unité de Biologie des Interactions Hôte-Parasite, CNRS ERL 9195, INSERM U1201, F-75015 Paris, France.

[4] Univ. Grenoble Alpes, INSERM, CEA, UMR BioSanté U1292, CNRS, CEA, FR2048 38000, Grenoble, France.

[5] Integrated Structural Biology Grenoble (ISBG) CNRS, CEA, Université Grenoble Alpes, EMBL, 71 avenue des Martyrs, F-38042, Grenoble, France.

[6] INRAE, Université François Rabelais de Tours, Centre Val de Loire, UMR1282 ISP, Laboratoire Apicomplexes et Immunité Mucosale, 37380 Nouzilly, France.

[†]These authors contributed equally to this work.

***** Correspondence to:
mohamed-ali.hakimi@univ-grenoble-alpes.fr - ORCiD: 0000-0002-2547-8233
alexandre.bougdour@univ-grenoble-alpes.fr - ORCiD: 0000-0002-5895-0020
christopher.swale@univ-grenoble-alpes.fr - ORCiD: 0000-0002-9739-7774

Spliceosome targeting by altiratinib leads to *Toxoplasma* and *Plasmodium* inhibition.

Key words: *Toxoplasma gondii*, *Plasmodium falciparum*, drug repurposing, kinase, splicing

Abstract

The apicomplexa comprise a large phylum of single-celled, obligate intracellular protozoa that include *Toxoplasma gondii*, *Plasmodium and Cryptosporidium spp* which infect humans and animals and cause severe parasitic diseases. Available therapeutics against these diseases are limited by suboptimal efficacy and frequent side effects, as well as the emergence and spread of resistance. We use a drug repurposing strategy and identified altiratinib, a compound originally developed to treat glioblastoma, as a promising drug candidate with broad spectrum activity against apicomplexans. Altiratinib is parasiticidal and blocks the development of intracellular zoites in the nanomolar range and with a high selectivity index when used against *T. gondii*. We have identified *Tg*PRP4K of *T. gondii* as the primary target of altiratinib using genetic target deconvolution, which highlighted key residues within the kinase catalytic site that conferred drug resistance when mutated. We have further elucidated the molecular basis of the inhibitory mechanism and species selectivity of altiratinib for *Tg*PRP4K as well as for its *P. falciparum* counterpart, *Pf*CLK3. Our data identified structural features critical for binding of the other *Pf*CLK3 inhibitor, TCMDC-135051. Consistent with the splicing control activity of this kinase family, we have shown that altiratinib can causes global disruption of splicing, primarily through intron retention in both *T. gondii* and *P. falciparum*. Thus, our data establish parasitic PRP4K/CLK3 as a potential pan-apicomplexan target whose repertoire of inhibitors can be expanded by the addition of altiratinib.

Introduction

Infectious diseases caused by apicomplexan parasites remain one of the leading causes of morbidity and mortality around the world, with even more devastating consequences in low-income countries, underscoring the need for effective medicines. *Plasmodium falciparum* causes malaria in over 240 million people worldwide and is responsible for more than 627 000 deaths in 2020 (*1*). Similarly, *Toxoplasma gondii*, the causative agent of toxoplasmosis, causes widespread zoonotic infection, with nearly one-third of the world's population being seropositive for this parasite. In healthy adults, the acute infection resolves rapidly, leaving a chronic, subclinical infection in some individuals. In the absence of sustained immunity, reactivation of latent forms of *T. gondii* leads to severe, life-threatening disease, as has been observed in AIDS, organ transplant and chemotherapy patients, with a high mortality rate in

the absence of treatment (*2*). More severe cases may also occur following congenital transmission of the parasite to an unborn child. In addition, *Toxoplasma gondii*, together with other coccidian parasites, e.g. *Eimeria* spp. And *Neospora caninum*, are of veterinary importance as they cause significant economic losses in livestock populations.

For many of these apicomplexa-mediated diseases, current treatments are suboptimal, and for some there are few, if any, alternatives. The current standard treatment of toxoplasmosis is based on a pyrimethamine-sulfadiazine combination but is hampered by severe side effects, especially in immunocompromised individuals (*3*). For malaria, artemisinin-based combination therapies (ACT) are currently used as first-line treatments in endemic countries worldwide, but the emergence and spread of resistance not only to artemisinin but also to other drug combinations is a growing threat (*1*). The ever-present threats of drug resistance have led to the search for other therapeutic alternatives. Older drugs have recently made a comeback by being repurposed for new diseases to accelerate drug development (*4*, *5*). After phenotypic screening for drug repurposing, new indications for existing drugs can be quickly identified and clinical trials can be rapidly conducted. Identifying the target and understanding the mechanism of action are critical bottlenecks in drug development, as these two phases provide the essential chemical basis for targeted inhibition and pave the way for chemical derivatization of the original drug candidate. Recent advances in genomics and target deconvolution strategies have addressed these problems and have ushered in a plethora of putative targets awaiting clarification.

Here, we report the identification of altiratinib from a chemical library that includes FDA-approved or phase I/ II clinical trial candidate drugs. Altiratinib exhibited potent, nanomolar, broad-spectrum anti-apicomplexan activity with a high selectivity index and had previously been in phase 1 clinical development for the treatment of invasive solid tumors, including glioblastoma (*6*, *7*). Using a genetic target deconvolution strategy, we identified *T. gondii* *Tg*PRP4K, the closest relative of the human splicing factor kinase PRP4 kinase (PRP4K/PRPF4B) and *Plasmodium falciparum* *Pf*CLK3 (*8*, *9*), as the primary target of altiratinib. In addition, we used an integrated structural biology approach to further elucidate the molecular basis of the mechanism of inhibition of altiratinib and characterized the remarkable selectivity of this drug for parasitic PRP4K/CLK3 enzymes. This kinase family plays a critical role in cell cycle progression by regulating pre-mRNA splicing in all eukaryotic lineages (*10-13*). Accordingly, altiratinib caused global disruption of splicing with exon

skipping, intron retention, and premature transcription termination in both *T. gondii* and *P. falciparum*, but not in *Cryptosporidium parvum*, in which the kinase has significantly divergent variations that may result in resistance to altiratinib. Our findings support this family of parasitic kinases as a promising apicomplexan target and highlight the structural determinants that explain the remarkable selectivity of altiratinib.

Results

A drug repurposing screen identifies altiratinib as a potent and selective apicomplexan inhibitor of parasite growth

To identify new drug candidates against toxoplasmosis and potential targets, we screened a small library of 514 approved drugs or drugs undergoing clinical trials for their ability to inhibit *T. gondii* tachyzoite growth. All compounds are structurally diverse, cell permeable, medically active, and commercially available (Table S1). Screening was performed in duplicate at 5 μM while pyrimethamine was used as a reference drug and blocked the growth of type I (RH) parasites as expected. The compounds that showed reproducible inhibition of parasite growth of >70% were selected for further testing (Fig. S1A; Table S1). Of the 514 compounds in the collection, 75 primary hits were found to inhibit parasite growth without detectable cytotoxicity to the host cell (Fig. 1A), preferentially targeting the cell cycle and tyrosine kinase/adaptor signaling pathways (Fig. S1B; Table S1). A second screen at 1 μM of the 84 compounds identified 14 molecules with EC_{50} in the nM range (Fig. 1B; Fig. S2). The most potent growth inhibitor we identified was altiratinib (DCC-2701, DP-5164, Fig. 1C) with an EC_{50} of 28 nM against tachyzoites, which is 11-fold lower than pyrimethamine (300 nM), the standard treatment for toxoplasmosis (Fig. 1D). Altiratinib-treated parasites were smaller than the control group and no longer divided, as no daughter cells were detectable (Fig. 1E). Plaque assays showed sustained inhibition of parasite growth, as plaques could no longer be detected in the presence of altiratinib, suggesting a defect in one or more steps of the lytic cycle (Fig. S3). Interestingly, we did not observe regrowth within 6 to 10 days after discontinuation of altiratinib, suggesting that the drug has a cidal effect in contrast to pyrimethamine (Fig. S3). Altiratinib also showed low host cytotoxicity compared with THZ1 used as a cytotoxic control (Fig. S1D), resulting in a high selectivity index (SI) with a value of 400 for human primary fibroblasts (Fig. 1F). Altiratinib was also effective in inhibiting the growth of coccidial parasites of veterinary importance such as *Eimeria tenella* (Fig. 1G) and *Neospora caninum* (Fig. 1H),

as well as *P. falciparum*, although its efficacy is lower compared with the antimalarial drug dihydroartemisinin (DHA) (Fig. 1i).

Altiratinib target deconvolution by EMS-based forward genetic screen identifies *Tg*PRP4K as a resistance gene

Altiratinib was originally identified to inhibit tumor growth and invasion in a bevacizumab-resistant glioblastoma mouse model and was in phase 1 clinical development for the treatment of invasive solid tumors. The drug was predicted to be a pan-tyrosine kinase inhibitor of MET, TIE2, VEGFR2, and TRK (*6, 7*), but none of these kinases are conserved in apicomplexa. Therefore, to explore the mechanism of action of altiratinib in *T. gondii*, we performed a forward genetic screen combining chemical mutagenesis and RNA sequencing, as previously described (*14*) (Fig. S1E). Altiratinib-resistant parasites were generated in 6 independent chemical mutagenesis experiments using 2.5 mM ethyl methanesulfonate (EMS) followed by selection in the presence of 300 nM altiratinib, i.e. 10-fold the EC_{50} value, for approximately 4 weeks. The resistant parasite lines were then cloned by limited dilution, and a single clone from each mutagenesis experiment (designated A to F) was analyzed by whole-genome RNA sequencing (RNA-Seq). To map the EMS-induced mutations conferring resistance to altiratinib, Illumina sequencing reads were aligned to the *T. gondii GT1* reference genome. Using the parental strain as a reference, single nucleotide variants (SNVs) were identified in the assembled sequences of the resistant mutants (see *Materials and Methods*). By focusing on mutations in coding sequences, a single gene, *TGGT1_313180*, contained SNVs that resulted in amino acid changes (F647S, L686F, L715F) not present in the parental strain in five of the six drug-resistant lines (Fig. 2, A and B; Table S2).

TGGT1_313180 encodes a 928 amino acid (aa) protein that has a predicted kinase domain in its C-terminus, hereafter referred to as *Tg*PRP4K (Fig. 2B). *Tg*PRP4K is phylogenetically related to the cyclin-dependent-like kinase family (CLK) (*15, 16*) and its closest homolog in humans is the splicing factor kinase PRP4 kinase (PRP4K or PRPF4B) and in *P. falciparum* is *Pf*CLK3 (*PF3D7_1114700*), a kinase that has been identified as a multistage cross-species antimalarial drug target (Fig. S4A) (*8, 9, 17*). Immunofluorescence analysis of intracellular parasites showed that *Tg*PRP4K is localized to nuclear speckle-like structures (Fig. 2C). *TgPRP4K* is essential for the lytic cycle of tachyzoites, as its genetic disruption results in a fitness score of -4.69 (*18*), and conditional knockdown of the kinase using the auxin-inducible

degron system (AID) dramatically impaired parasite growth (Fig. 2D) in agreement with a recent study (*19*).

Surprisingly, the altiratinib-resistant parasite line from mutagenesis F has a wild-type (WT) allele of *Tg*PRP4K and a mutation E1325K in *Tg*PRP8, a protein located in the catalytic core of the spliceosome that has been shown to interact with PRP4K in *Schizosaccharomyces pombe* to facilitate spliceosome activation (*20*, *21*). This reinforces the possibility that the PRP4K-PRP8 complex is at the basis for the anti-*Toxoplasma* activity of altiratinib. The specific association between *Tg*PRP4K and *Tg*PRP8 was then confirmed by FLAG affinity immunoprecipitation and mass spectrometry (MS)-based proteomic analyzes using knock-in parasite lines expressing a tagged version of each protein (Table S3; Fig. S4, B and C). Other partners have been identified as pre-mRNA splicing proteins constitutive of the core spliceosome, such as U2 snRNP proteins and U5 snRNP proteins, including the RNA helicase Brr2 and Snu114, which forms a pocket enclosing the catalytic RNA network of activated spliceosomes (Fig. S5) (*21*, *22*). Known pre-mRNA splicing factors were also purified along with PRP4K and PRP8 (Table S3; Fig. S4, B and C; Fig. S5). *Tg*PRP4K was found in a high molecular-weight complex (~500 kDa; fractions 24–26) that withstood stringent salt conditions and partially co-eluted with the *Tg*PRP8-containing spliceosome, which migrates by size exclusion chromatography with an apparent molecular weight of ~900 kDa (fractions 18-20) (Fig. S4, B and C).

Single mutations within *Tg*PRP4K confer resistance to altiratinib

To confirm that the mutations found in *Tg*PRP4K and *Tg*PRP8 were sufficient to confer resistance to altiratinib, we used the CRISPR/Cas9 system in conjunction with homology-directed repair, to reconstruct each of the etiological mutations into the susceptible parental *T. gondii* strain (*14*). Parasites were cotransfected with a vector expressing the Cas9 endonuclease and a synthetic guide RNA (sgRNA) targeting either *TgPRP4K* or *TgPRP8*, and the corresponding homologous single-stranded donor oligonucleotides (ssODN) as repair templates (Fig. S6A). After altiratinib selection, the resistant parasites were cloned, and DNA sequencing confirmed that the mutations were properly introduced at the *TgPRP4K* locus (Fig. S6B). Note that despite numerous attempts, allelic substitution for *TgPRP8* could not be achieved, suggesting that the *Tg*PRP8 (E1325K) mutation alone does not confer resistance to altiratinib and was not investigated further. Compared with WT parasites, mutant strains edited

for *TgPRP4K* (mutations F647S, L686F, and L715F) significantly decreased sensitivity to altiratinib by 50- to 180-fold (Fig. 2, E to G; Fig. S6C), suggesting that resistance to altiratinib correlates with *Tg*PRP4K activity. In addition, the CRISPR/Cas9-edited lines had altiratinib resistance levels at least as high as the EMS-mutagenized clones (Fig. S7; Table S2). This suggests that the reconstructed *Tg*PRP4K mutations fully recapitulate the resistance phenotype originally observed in the mutagenized lines, and that it is unlikely that other secondary mutations are involved in the resistance mechanism. It is worth noting that the CRISPR/Cas9-edited parasite with the F647S mutation exhibited a higher level of resistance to altiratinib than its mutant counterpart, most likely due to overall growth failure of the latter (Fig. S7).

Structural studies uncover the mechanism of action of altiratinib on *Tg*PRP4K

To unravel the molecular mechanism of action of altiratinib inhibition, we expressed the predicted kinase domain of *Tg*PRP4K in the WT and L715F variant versions by removing the intrinsically disordered region at the N-terminus (Fig. S8A). Both recombinant proteins were produced in satisfactory yields, with the notable difference being a higher size homogeneity of the L715F mutant (Fig. S8B) when analyzed by size exclusion chromatography coupled to laser light scattering (SEC-MALLS). The same sample did not display a double band that can be seen in the WT (Fig. S8C) and was also observed in Flag-purified human WT PRPF4B as a result of posttranslational modifications (*23*). The L715F mutation is peculiar because it centered on the DFG (Asp-Phe-Gly) motif, which is a DLG (Asp-Leu-Gly) in apicomplexan parasites. DFG (or DLG in a subset of kinases, such as RIPK1) is a highly conserved peptidic motif found in most human kinases and is critical for allosteric placement of the activation loop. Using a thermal stability assay and a thermophoresis titration assay, we could show a direct stabilizing effect (delta Tm of 11°C) and binding (apparent Kd of 64 nM) of altiratinib with the WT *Tg*PRP4K kinase domain (Fig. 3, A and B). Counterintuitively though, the L715F mutation does not decrease altiratinib binding, but instead increases binding affinity (Fig. 3, A and B). This not only increases the apparent Kd value (26 nM), but also increases the stabilizing effect of the compound *in vitro* compared to WT (with a ΔTm of 15 °C). This surprising observation highlights an unusual resistance mechanism that should somehow compensate for the inhibitory mechanism, regardless of the binding affinity of the compound. Using this point mutant, we successfully co-crystallized *Tg*PRP4K in complex with altiratinib and obtained high-resolution diffraction to 2.3Å (pdb id: 7Q4A, Table S4). A molecular replacement solution was found with the human homolog of PRPF4B kinase domain (pdb id: 6CNH), which shares 47% sequence

identity with *Tg*PRP4K. The structure solution showed *Tg*PRP4K crystallizing as a dimer with the catalysis cavities facing each other (Fig. S9A). The monomer B exhibited more complete density within the flexible regions, so all further structural representations are based on this monomer. The activation loop was fully assembled in our model and occupies a DFG "out" conformation while the tyrosine 729 is phosphorylated in this structure (Fig. 3C, Fig. S9B and C). Interestingly, this phospho-tyrosine is central to the ability of *Tg*PRP4K to crystallize under these conditions, as it forms numerous crystal contacts with other symmetry-related molecules (Fig. S9B).

The activation loop displays an alpha helix (Ile 726 to Tyr 735) that appears to be unique to *T. gondii* PRP4K when compared to the human ortholog, which was only ever crystallized in DFG "in" conformations and is largely a random coil in this state (Fig. 3C, Fig. S9C). Compared to the human ortholog in its global structure, *Tg*PRP4K is structurally conserved, with minor structural differences in the C-terminal portion (aa 840 to 854) of the kinase domain (Fig. S9C). The structure also reveals a C-terminal antiparallel short beta strand that, to our knowledge, is unique to the PRP4K kinase lineage (Fig. 3C) and is also structurally conserved in the human ortholog (Fig. S9C), although sequence conservation for this region is very low.

Electron density for altiratinib was clearly visible in our crystal structure and interacts in the ATP-binding pocket located at the interface between the N- and C-lobes (Fig. 3C), with the DFG motif and the G-rich loop closing off this cavity. It is noteworthy that both monomers display strong electron density for altiratinib, allowing us to confidently assign the entire molecule (Fig. S10A). More detailed analysis revealed that the interaction of the compound within the cavity relies on numerous hydrophobic interactions (Fig. 3D; Fig. S10, B and C), which can be divided into three distinct zones. The first zone, consisting of a cyclopropane-carbonylamino group connecting a pyridine ring, interacts mainly with side chains W649, L650, W651, L702 and A595 (Fig. 3D, Fig. S10C). Hydrogen bonds also form with the carbonyl and amide groups of the leucine 650, and most of these residues form the ATP-binding hinge region, leading to the deeper allosteric pocket. The second zone of altiratinib is central and consists mainly of a difluorophenyl ring stacked between the two phenylalanines 647 and 715 (the DFG central residue, which is a leucine in wild type *Tg*PRP4K) (Fig. 3D), with one of the fluorine groups interacting with the sulfur group of C713 (Fig. S10C). These interactions ensure that the activation loop remains in this « out » position. Finally, the last part of altiratinib which

encompasses a cyclopropane-1,1-dicarboxamide leading to a fluorophenyl ring, is buried deep in the allosteric cavity and interacts with multiple residues within the C-lobe, notably the glutamic acid 612 and leucine 616 and 619, which line up on the C-alpha-helix (Fig. 3D, Fig. S10C). Other interactions are mediated by I630 and L686, as well as the H693, which belongs to the canonical HxD triad that is a H/A/D in PRP4K proteins. Only one residue within the N-lobe, the catalytic lysine K597, forms a hydrogen bond with the central carboxy group. Using this structure, we can now rationalize the consequences of the resistance mutations triggered by our EMS screen. All of the point mutations we obtained involve residues that interact directly with altiratinib, whereas the direct mechanisms of resistance are likely quite different (Fig. 3E). The L686F mutation logically introduces a steric hindrance for the fluorophenyl ring by significantly increasing the size of the side-chain. The other two resistance-conferring mutations, F647S and L715F, involve residues in direct interaction and at opposite sides of the central difluorophenyl ring. F647S probably strongly decreases hydrophobic stacking, while we have evidence that the mutation L715F does not cause steric hindrance but, on the contrary, probably increases hydrophobic stacking of the difluorophenyl ring. As such, most of the mutated residues are highly conserved elements found in both *Hs*PRPF4B and *Tg*PRP4K (the L715F is a significant divergence but does not negatively affect compound binding) and are unlikely to be involved in interspecies binding selectivity. Altiratinib is not recognized as an inhibitor of PRPF4B in human cells, as it was originally designed to inhibit the kinases MET, TIE2 (TEK), and VEGFR2 (KDR) (*6, 7*). Of the residues involved in binding to altiratinib, most are strictly conserved among PRPF4B orthologs (Fig. 3E), but the hinge region has residues (W649 and W651) that diverge considerably from the human ortholog, being replaced by a proline and serine, respectively.

Hinge region residue 649 controls species specificity of altiratinib towards *Tg*PRP4K

The superposition of the human and *T. gondii* PRPF4B/PRP4K structures makes it clear that the hinge region has a consistent backbone structure despite significant differences in side chain composition (Fig. 4A). More importantly, this overlay shows that the change from W649 to P769 would affect the main hydrophobic component that stacks the cyclopropane-carbonylamino and pyridin groups of altiratinib. A similar, albeit lesser, role can also be attributed to W651, whose equivalent residue in humans is S771 and likely reduces the hydrophobic caging potential toward altiratinib. To test the significance of residue W649, we used the same CRISPR-Cas9 complementation approach for SNV validation to generate a "humanized" mutant W649/P that requires a codon change from TGG to CCG (Fig. 4B). The

probability of such a change occurring in EMS mutagenesis is low because it requires a simultaneous alteration of two nucleotides. This substitution is not prevalent in EMS mutagenesis, which preferentially alkylates G residues (*24*). Interestingly, this artificial humanization produced parasites that were resistant to altiratinib (Fig. 4, C to E) and had an EC50 of 3.5 μM, which is comparable to the mutations using the EMS approach. Using *Tg*PRP4K WT, L715F and W649P expressed in insect cells, we were able to probe the *in vitro* consequences of these two different mutations on the ability of the protein to interact with altiratinib. Using an indirect thermal shift assay and a thermophoresis approach (Fig. 4, F to H), we demonstrated that the hydrophobic stacking of W649 is essential for altiratinib binding, as almost no stabilization is observed in the presence of altiratinib (delta Tm of 3 °C), compared to WT PRPF4B (Delta Tm of 11°C, Fig. 3A), while the apparent Kd measured in thermophoresis transitions from 64 nM to not measurable (Fig. 3B and Fig. 4G).

Finally, we tested these sets of recombinant wild-type and mutant *Tg*PRP4K proteins to assess the inhibitory effect of altiratinib on *in vitro* endpoint kinase activity using a reporter assay for ATP content and PRP31 peptide as substrate. In this context, WT *Tg*PRP4K shows measurable kinase activity and exhibits the highest sensitivity to altiratinib with an apparent IC50 of 13 nM (Fig. 4i). The L715F mutant binds with higher affinity to altiratinib but is significantly less sensitive with an apparent IC50 of 62 nM. The W649P mutation brings the greatest tolerance to altiratinib, as the apparent IC50 now ranges at more than 300 nM (Fig. 4i).

Chemically induced inactivation of *Tg*PRP4K activity disturbs pre-mRNA splicing in *T. gondii*

Since it has been proposed that the human kinase PRPF4B and *Pf*CLK3 regulate RNA splicing (*8*, *10*), we examined transcriptional changes in the parental parasite RH and in the drug-resistant strains L715F and W649P in response to exposure to altiratinib using nanopore long-read direct RNA sequencing (DRS), a technology well suited for determining the full repertoire of mRNA species, including alternative splicing isoforms and divergent patterns, if present. The most obvious effect was that a substantial number of genes (n=2400) showed altered mRNA expression, of which 784 were induced and 1616 repressed when the parent strain was treated with altiratinib, whereas no significant changes were observed in the two mutant strains exposed to the drug (Fig. 5A). This confirms that altiratinib disrupts mRNA transcription, which was expected, but also that the drug specifically targets *Tg*PRP4K, as both mutations not only confer resistance (Fig. 2, D to F) but also restore gene expression to the untreated state

(Fig. 5A). Having identified isoforms with high confidence using the Nanopore data, we used FLAIR (Full-Length Alternative Isoform Analysis of RNA) (*25*) as a framework for analyzing differential isoform usage in wild-type and mutant strains left untreated or exposed to altiratinib. The most important transcriptional phenotype was the change in pre-mRNA splicing dynamics associated with inhibition of *Tg*PRP4K exclusively in WT parasites (Fig. 5B). At many *loci*, chemical inactivation of *Tg*PRP4K was accompanied by complete retention of the second intron (e.g., *TGME49_214940*; Fig. 5, B and D) or intron retention and exon skipping at the same *loci* (e.g., *TGME49_211420* and *TGME49_247350*; Fig. 5C; Fig. S11A). When an intron is spliced, it rapidly promotes splicing of subsequent introns, whereas when splicing is hindered, subsequent introns tend to be retained, leading to the concept of 'all or none' splicing (*26*, *27*). Consistent with this concept, we regularly observed a global collapse of splicing along the entire transcript (e.g., *TGME49_208450*; Fig. S11B) after drug treatment.

Since splicing is predominantly co-transcriptional, we also observed that intron retention leads to premature transcriptional termination (e.g., *TGME49_278940*; Fig. S11C). At the transcriptome level, intron retention is the predominant aberrant splicing event found in altiratinib-treated WT tachyzoites in contrast to the host cells they infect, underscoring the high degree of selectivity of altiratinib (Fig. 5E). Upon closer inspection, we found that intron retention leads to premature termination of translation due to frameshifts, which may ultimately lead to altered function of the protein-coding gene. In addition, aberrant isoforms are degraded, as indicated by the lower read rates at some *loci*, likely through nonsense-mediated decay (NMD), a quality control mechanism that eliminates transcripts with a premature termination codon. In this way, treatment with altiratinib leads to the production of defective proteins that ultimately affect parasite survival.

Altiratinib also causes mis-splicing in *P. falciparum* but not in *C. parvum*, which has a divergent PRP4K ortholog

Because altiratinib was active against a wide range of apicomplexans (Fig. 1) and the PRPK4/CLK3 family was well conserved within the phylum, we wondered whether the drug might inhibit splicing in other parasites of the phylum. We first examined transcriptional changes of red blood cells infected with *P. falciparum* after treatment with altiratinib using Nanopore DRS. All types of splicing defects that we had observed in *T. gondii* were also present in *P. falciparum*, such as exon skipping, intron retention, and premature transcription

termination (Fig. 6A; Fig. S12, A to C), with a general trend toward global splicing collapse along the entire transcript, with premature mRNAs being highly susceptible to NMD degradation (Fig. S12, A to C), As with *T. gondii*, markedly increased intron retention is a conserved phenomenon in *P. falciparum* exposed to altiratinib (Fig. 6B). These results underscore the potential targeting by altiratinib of *Pf*CLK3 (*PF3D7_1114700*), a kinase that is essential for *P. falciparum* survival in red blood cells and plays a critical role in regulating RNA splicing of the malaria parasite (*8, 9*). We then took the opportunity to test the drug on *Cryptosporidium parvum*, a parasite of the phylum that differs from others in having a significantly divergent ortholog of PRP4K/CLK3 (*cgd8_5180*, Fig. S4A), specifically the resistance-conferring DFG motif instead of the DLG motif found in *T. gondii* and *P. falciparum,* but also several significant mutations at other altiratinib-interacting residues (L719 to F, W651 to H, and C713 to S) that may strongly affect the binding selectivity of altiratinib (Fig. S12, D and E). As expected, we observed no defects in mRNA splicing in *C. parvum* exposed to altiratinib (Fig. 6, C and D; Fig. S12D), again confirming the selectivity of the drug for PRP4K/CLK3 with a DLG motif and ruling out off-target activities (Fig. S12E).

Assessing the ins and outs of CLK3/PRP4K inhibition by altiratinib or TCMDC-135051

To further confirm *P. falciparum Pf*CLK3/PRP4K as a target of altiratinib, we expressed the WT *Pf*PRP4K kinase domain to probe this biochemical interaction (Fig. S13A). Using the previously described thermal shift assay, we found that altiratinib indeed stabilizes *Pf*CLK3, albeit with a weaker potential, the delta Tm is of 4°C, compared to *Tg*PRP4K, which has a delta Tm of 11°C (Fig. 6E). Interestingly, however, when probing the TCMDC-135051 compound, a recently discovered inhibitor of PfCLK3 (*9*), we observed a reversed trend with a stronger stabilizing effect on *Pf*CLK3 with a delta Tm of 10°C instead of 7°C for *Tg*PRP4K (Fig. 6E). These results highlight two important aspects. First, we confirm that TCMDC-135051 likely binds the active site of *Pf*CLK3 as the energy requirements for such a stabilizing effect would probably only occur within a buried cavity strongly interacting with the compound. Second, this also highlights that there may still be some species selectivity between the two compounds. As we were unable to crystallize *Pf*CLK3 in the bound or unbound state, we used alphafold2 (*28*) within collabfold (*29*) to create a model that we superposed to our crystallographic structure and manually docked TCMDC-135051, taking advantage of the structural homology to other hinge regions binders containing a 7-azaindole scaffold (Fig. S13B, as initially proposed in *9*). In this modeling (Fig. 6F), we observe that most of the PRP4K/CLK3 hinge

region is conserved between *P. falciparum* and *T. gondii*, in particular residues W649/W651 in *Tg*PRP4K, which are also fully conserved in *Pf*CLK3 (W446/W448) and likely also have an important impact on the selectivity of TCMDC-135051, particularly through hydrophobic stacking. However, the conformation of the activation loop is not consistent with the binding of TCMDC-135051 in the *Tg*PRP4K structure (Fig. 6F), indicating potential differences in the activation loop conformation that may differ between TCMDC-135051 and altiratinib.

Discussion

Our studies define altiratinib as a promising apicomplexan drug candidate effective against the human pathogens *T. gondii* and, with lesser efficacy, *P. falciparum*, as well as *N. caninum* and *E. tenella* of veterinary interest. Using genetic, structural and transcriptional approaches, we have shown that repurposing of altiratinib disrupts mRNA splicing in *T. gondii* and *P. falciparum* by targeting the kinase core of PRP4K/CLK3. The induced splicing defects are so extensive that they lead to irreversible inhibition in the nanomolar range of rapidly proliferating apicomplexan zoites in cellular assays. Using a genetic target-deconvolution strategy, we have highlighted key residues involved in binding to altiratinib. Unexpectedly, this has allowed us to crystallize and resolve the first structure of a previously elusive apicomplexan kinase PRP4K/CLK3. This co-crystal structure allows us to assign the electron density of altiratinib, located at the interface between the N- and C-terminal lobes and occupying both the ATP-binding site and the allosteric pocket, a singular type of binding that holds PRP4K in a DFG-out conformation consistent with inhibition of the type II kinases. The structural data have clarified many unanswered questions related to the species selectivity of altiratinib, as we now know that its ability to discriminate the human ortholog and bind the parasitic PRP4K/CLK3 is constrained by residues W649/W651 in the hinge region (Fig. 4A), which have diverged significantly and are also likely critical for binding of the recently discovered *Pf*CLK3 inhibitor TCMDC-135051 (Fig. 6F) (*8*, *9*). Another important divergence is the shift from DFG to DLG that has occurred between mammals and some apicomplexans. DLG is indeed associated with inactive or less active kinases such as ROR2 (*30*, *31*), and the selective pressure that led to this mutation is not yet clear, as DFG-mutated tachyzoites behave normally in cell cultures (Fig. 2, D to F). DLF conversion to DFG results in resistance to altiratinib, both *in vivo* and *in vitro* activity assays. This observation, although counterintuitive, is not unique, as other resistance-conferring mutations in *Abl*, *RET*, and *EGFR* have been shown to promote resistance by increasing kinase activity without altering the binding properties of the drug (*32*-*34*). This likely

gain in activity is sufficient to resist altiratinib both *in vivo* and *in vitro*, although binding affinities are increased. Our work highlights the utility of drug repurposing and provides structural mechanistic insights into understanding how the PRP4K/CLK3 family is susceptible to selective pharmacological inhibition by small drug-like molecules. This opens new opportunities to chemically improve existing molecules to optimize pathogen killing via the PRP4K/CLK3 pathway.

However, some open questions and study limitations remain. Although the evidence for a direct interaction between altiratinib and PRP4K/CLK3 and drug-induced mis-splicing is overwhelming, the possibility that *Tg*PRP4K acts as a resistance gene cannot be ruled out. Moreover, the true mechanism of spliceosome inhibition is still in question, as PRP4K not only plays a role in pre-B spliceosome activation by phosphorylating other components of PRP, notably PRP6 and PRP31 (*10*), but also structurally integrates the complex (*21*) and contacts the RNase PRP8, which may be allosterically involved in its activity. Inhibition of activity or conformational entrapment (or both) may therefore be the key to proper inhibition. Furthermore, the *in vitro* inhibition assay had to be performed with protein concentrations higher than the apparent IC_{50} (107 nM) and display inherent differences in intrinsic activity (between wild-type and mutated recombinant *Tg*PRP4K). Although the relative distribution of the $IC50_{app}$ values confirms the trend toward resistance, IC_{50} values are influenced by stoichiometric (tight) binding kinetics and may be overestimated in this context.

Our structural model is also built on a L715F mutated *Tg*PRP4K which has provided us with a stable crystal system. While the placement of altiratinib will not change, the activation loop dynamics are probably different in the wild-type context. *Pf*CLK3 has been identified as a multistage cross-species malarial drug target and TCMDC-135051 a drug candidate with a high curative and transmission-blocking potential (*8*, *9*). Altiratinib and TCMDC-135051 have a very different chemical space (Fig. S13B) and although they probably rely on comparable elements within the hinge region to selectively bind apicomplexan PRP4K/CLK3, species selectivity is still present, possibly due to differences in the dynamics of the activation loop with which binding is compatible. Dual (SAR)-directed optimization will therefore open the possibility of developing a pan-apicomplexan therapy based on the altiratinib/TCMDC-135051 combination.

Materials and Methods

Study Design

This study includes three sequential phases. An *in vitro* phenotypic screen using *T. gondii* tachyzoites infecting single-layered cells to identify potent inhibitors within a small library of repurposable drugs. The second phase was to determine the inhibitory properties of the lead compound altiratinib and identify resistance-conferring genes by chemical mutagenesis of *T. gondii*, mapping of point mutations, and complementation in a wild-type background. The third phase was to confirm the mechanism of action of altiratinib on *Tg*PRP4K by *in vitro* biophysical methods, experimental structural biology, and functional transcriptomics in several apicomplexan parasites cultured *in vitro*. Sample sizes were based on similar experiments in the literature and are indicated in the figure legends. Whenever possible, replicate or triplicate measurements were performed. Proteomic, transcriptomic or structural experimental data were deposited in curated databases when available. This study was not blinded.

***Toxoplasma gondii*, *Plasmodium falciparum* and human cell culture.** Human primary fibroblasts (HFFs, ATCC® CCL-171™) were cultured in Dulbecco's Modified Eagle Medium (DMEM) (Invitrogen) supplemented with 10% heat inactivated Fetal Bovine Serum (FBS) (Invitrogen), 10 mM (4-(2-hydroxyethyl)-1-piperazine ethanesulphonic acid) (HEPES) buffer pH 7.2, 2 mM L-glutamine and 50 µg/ml of penicillin and streptomycin (Invitrogen). Cells were incubated at 37°C in 5% CO2. The *Toxoplasma* strains used in this study and listed in Table S5 were maintained *in vitro* by serial passage on monolayers of HFFs. The cultures were free of mycoplasma, as determined by qualitative PCR. *P. falciparum* parasites were cultured using standard culture conditions (*35*). The drug sensitive laboratory strain 3D7 was used in this study.

***Toxoplasma gondii* genome editing.** Targeted genome modifications were performed using the *T. gondii* adapted CRISPR/Cas9 system as previously described (*36*). Recombinant parasites harboring allelic replacement for PRP4K^{F647S}, PRP4K^{L686F}, PRP4K^{L715F}, and PRP4K^{W649P} were generated by electroporation of the *T. gondii* RH NLuc strain with pTOXO_Cas9CRISPR vectors targeting the *PRP4K* coding sequence (sgPRP4K^{F647S}, sgPRP4K^{L686F}, sgPRP4K^{L715F}) and their respective donor single-stranded oligo DNA nucleotides (ssODNs) carrying respective nucleotide substitutions (PRP4K^{F647S}_donor,

PRP4K^{L686F}_donor, PRP4K^{L715F}_donor; Table S5) for homology-directed repair. Recombinant parasites were selected with 300nM altiratinib prior to subcloning by limited dilution, and allelic replacement was verified by sequencing of *T. gondii TgPRP4K* genomic DNA.

***Toxoplasma gondii* random mutagenesis**. Parasites (RH strain) were chemically mutagenized as previously described (*14*), with the following modifications. Briefly, ~10^7 tachyzoites growing intracellularly in HFF cells in a T25 flask were incubated for 4 h at 37°C in 0.1% FBS DMEM growth medium containing either 2.5 mM ethyl methanesulphonate (EMS) at final concentration or the appropriate vehicle controls. After exposure to the mutagen, parasites were washed three times with PBS, and the mutagenized population was allowed to recover in a fresh T25 flask containing an HFF monolayer in the absence of drug for 3–5 days. The released tachyzoites were then inoculated into fresh cell monolayers in medium containing 300 nM of altiratinib and incubated until viable extracellular tachyzoites emerged 8–10 days later. Surviving parasites were passaged once more under continued altiratinib treatment and cloned by limiting dilution. The cloned mutants were each isolated from 6 independent mutagenesis experiments. Thus, each flask contained unique SNV pools.

Direct RNA sequencing by nanopore. The mRNA library preparation followed the SQK-RNA002 kit (Oxford Nanopore) recommended protocol, the only modification was the input mRNA quantity increased from 500 to 1000 ng, all other consumables and parameters were standard. Final yields were evaluated using the Qubit HS dsDNA kit (Thermofisher Q32851) with minimum RNA preps reaching at least 150 ng. For all conditions, sequencing was performed on FLO-MIN106 flow cells either using a MinION MK1C or MinION sequencer. All datasets were subsequently basecalled with a Guppy version higher than 5.0.1 with a Qscore cutoff > 7. Long read alignment were performed by Minimap2 as previously described (*37*). Alignments were converted and sorted using Samtools.

Software and Statistical analyses. Volcano plots, scatter plots, and histograms were generated with Prism 7. Structural representations of *Tg*PRP4K and *Pf*PRP4K/CLK3 were performed using UCSF-Chimera while the schematic representation of altiratinib interaction network was computed using Ligplot.

List of Supplementary Materials

Supplementary Materials and Methods and references

Fig. S1. Identification of altiratinib by a medium-throughput screening of an FDA-approved library.

Fig. S2. Chemical structures of the 14 compounds selected for their efficacy in inhibiting growth of *T. gondii*.

Fig. S3. Representation of T. gondii cytotoxicity after incubation with drugs.

Fig. S4. Origin and interactome of TgPRP4K.

Fig. S5. Domain architectures of proteins purified together with PRP4K and PRP8.

Fig. S6. Identification and validation of the molecular target TgPRP4K.

Fig. S7. Comparison of altiratinib resistance in EMS-mutagenized and CRISPR/Cas9-edited lines.

Fig. S8. Insect-cell recombinant expression of TgPRP4K.

Fig. S9. Crystal structure specificities of TgPRP4K.

Fig. S10. Altiratinib binding site and interaction network.

Fig. S11. DRS examples of altiratinib induced splicing defects in *Toxoplasma gondii*.

Fig. S12. DRS examples of altiratinib treatment on *P. falciparum* and *C. parvum*.

Fig. S13. Biochemistry of recombinant PfPRP4K and chemical structure comparison of altiratinib and TCMDC-135051.

Table S1. Table describing the compound library and the selected molecules.

Table S2. RNA-Seq Analysis of the EMS-Induced Drug-Resistant Lines of T. gondii.

Table S3. Mass spectrometry-based characterization of the interactomes of PRP4K and PRP8.

Table S4. Statistics of crystallographic data.

Table S5. Description of *T. gondii* strains, plasmids and primers.

Data File 1. Full PDB X-ray structure validation report of crystal structure of Toxoplasma TgPRP4K with altiratinib (pdb id: 7Q4A).

References and Notes

1. WHO. World Malaria Report 2021. Who vol. 73 (2021).
2. J. G. Montoya, O. Liesenfeld, Toxoplasmosis. *Lancet* **363**, 1965–1976 (2004).
3. I. R. Dunay, K. Gajurel, R. Dhakal, O. Liesenfeld, J. G. Montoya, Treatment of toxoplasmosis: historical perspective, animal models, and current clinical practice. *Clin. Microbiol. Rev.* **31**, e00057-17 (2018).

4. K. Bessoff, A. Sateriale, K. K. Lee, C. D. Huston, Drug repurposing screen reveals FDA-approved inhibitors of human HMG-CoA reductase and isoprenoid synthesis that block Cryptosporidium parvum growth. *Antimicrob Agents Chemother*. **57**,1804-1814 (2013).
5. M. Xu, E. M. Lee, Z. Wen, Y. Cheng, W. K. Huang, X. Qian, J. Tcw, J. Kouznetsova, S. C. Ogden, C. Hammack, F. Jacob, H. N. Nguyen, M. Itkin, C. Hanna, P. Shinn, C. Allen, S. G. Michael, A. Simeonov, W. Huang, K. M. Christian, A. Goate, K. J. Brennand, R. Huang, M. Xia, G. L. Ming, W. Zheng, H. Song, H. Tang, Identification of small-molecule inhibitors of Zika virus infection and induced neural cell death via a drug repurposing screen. *Nat Med*. **22**, 1101-1107 (2016).
6. Y. Kwon, B. D. Smith, Y. Zhou, M. D. Kaufman, A. K. Godwin, Effective inhibition of c-MET-mediated signaling, growth and migration of ovarian cancer cells is influenced by the ovarian tissue microenvironment. *Oncogene* **34**, 144–153 (2015).
7. B. D. Smith, M. D. Kaufman, C. B. Leary, B. A. Turner, S. C. Wise, Y. M. Ahn, R. J. Booth, T. M. Caldwell, C. L. Ensinger, M. M. Hood, W. P. Lu, T. W. Patt, W. C. Patt, T. J. Rutkoski, T. Samarakoon, H. Telikepalli, L. Vogeti, S. Vogeti, K. M. Yates, L. Chun, L. J. Stewart, M. Clare, D. L. Flynn, Altiratinib Inhibits Tumor Growth, Invasion, Angiogenesis, and Microenvironment-Mediated Drug Resistance via Balanced Inhibition of MET, TIE2, and VEGFR2. *Mol Cancer Ther.* **9,** 2023-2034 (2015).
8. M. M. Alam, A. Sanchez-Azqueta, O. Janha, E. L. Flannery, A. Mahindra, K. Mapesa, A. B. Char, D. Sriranganadane, N. M. B. Brancucci, Y. Antonova-Koch, K. Crouch, N. V. Simwela, S. B. Millar, J. Akinwale, D. Mitcheson, L. Solyakov, K. Dudek, C. Jones, C. Zapatero, C. Doerig, D. C. Nwakanma, M. J. Vázquez, G. Colmenarejo, M. J. Lafuente-Monasterio, M. L. Leon, P. H. C. Godoi, J. M. Elkins, A. P. Waters, A. G. Jamieson, E. F. Álvaro, L. C. Ranford-Cartwright, M. Marti, E. A. Winzeler, F. J. Gamo, A. B. Tobin, Validation of the protein kinase Pf CLK3 as a multistage cross-species malarial drug target *Science* **365**(6456):eaau1682 (2019).
9. A. Mahindra, O, Janha, K. Mapesa, A. Sanchez-Azqueta, M. M. Alam, A. Amambua-Ngwa, D. C. Nwakanma, A. B. Tobin, Jamieson AG. Development of Potent PfCLK3 Inhibitors Based on TCMDC-135051 as a New Class of Antimalarials. *J Med Chem*. **63**, 9300-9315 (2020).
10. M. Schneider, H. H. Hsiao, C. L. Will, R. Giet, H. Urlaub, R. Lührmann, Human PRP4 kinase is required for stable tri-snRNP association during spliceosomal B complex formation. *Nat Struct Mol Biol.* **17**, 216-221 (2010).

11. M. Lützelberger, N. F. Käufer, The Prp4 Kinase: Its Substrates, Function and Regulation in Pre-mRNA Splicing. In: Dr. Huang Cai (Ed.), editor. Protein Phosphorylation in Human Health: InTech. (2012).
12. D. P. Corkery, A. C. Holly, S. Lahsaee, G. Dellaire, Connecting the speckles: Splicing kinases and their role in tumorigenesis and treatment response. *Nucleus* **6**, 279-88 (2015).
13. D. Eckert, N. Andrée, A. Razanau, S. Zock-Emmenthal, M. Lützelberger, S. Plath, H. Schmidt, A. Guerra-Moreno, L. Cozzuto, J. Ayté, N. F. Käufer, Prp4 Kinase Grants the License to Splice: Control of Weak Splice Sites during Spliceosome Activation. *PLoS Genet*. **12**, e1005768 (2016).
14. V. Bellini, C. Swale, M. P. Brenier-Pinchart, T. Pezier, S. Georgeault, F. Laurent, M. A. Hakimi, A. Bougdour, Target Identification of an Antimalarial Oxaborole Identifies AN13762 as an Alternative Chemotype for Targeting CPSF3 in Apicomplexan Parasites. *iScience.* **23**, 101871 (2020).
15. E. Talevich, A. Mirza, N. Kannan, Structural and evolutionary divergence of eukaryotic protein kinases in Apicomplexa. *BMC Evol. Biol*. **11**, 321 (2011).
16. Z. Zhou, X. D. Fu, Regulation of splicing by SR proteins and SR protein-specific kinases. *Chromosoma* **122**, 191–207 (2013).
17. S. Agarwal, S. Kern, J. Halbert, J. M. Przyborski, S. Baumeister, T. Dandekar, C. Doerig, G. Pradel, Two nucleus-localized CDK-like kinases with crucial roles for malaria parasite erythrocytic replication are involved in phosphorylation of splicing factor. *J. Cell. Biochem.* **112**, 1295–1310 (2011).
18. S. M. Sidik, D. Huet, S. M. Ganesan, M. H. Huynh, T. Wang, A. S. Nasamu, P. Thiru, J. P. J. Saeij, V. B. Carruthers, J. C. Niles, S. Lourido, A Genome-wide CRISPR Screen in Toxoplasma Identifies Essential Apicomplexan Genes. *Cell.* **166**, 1423-1435 (2016).
19. V. V. Lee, S. Seizova, P. J. McMillan, E. McHugh, C. J. Tonkin, S. A. Ralph, Identification and characterisation of splicing regulators in Toxoplasma gondii. https://www.biorxiv.org/content/10.1101/2021.06.27.450092v3
20. C. A. Bottner, H. Schmidt, S. Vogel, M. Michele, N. F. Käufer, Multiple genetic and biochemical interactions of Brr2, Prp8, Prp31, Prp1 and Prp4 kinase suggest a function in the control of the activation of spliceosomes in Schizosaccharomyces pombe. *Curr Genet.* **48**, 151-61 (2005).
21. C. Charenton, M. E. Wilkinson, K. Nagai, Mechanism of 5' splice site transfer for human spliceosome activation. *Science.* **364**, 362-367 (2019).

22. K. Bertram, D. E. Agafonov, O. Dybkov, D. Haselbach, M. N. Leelaram, C. L. Will, H. Urlaub, B. Kastner, R. Lührmann, H. Stark, Cryo-EM Structure of a Pre-catalytic Human Spliceosome Primed for Activation. *Cell* **170**, 701–713 (2017).
23. G. Dellaire, E. M. Makarov, J. J. Cowger, D. Longman, H. G. Sutherland, R. Lührmann, J. Torchia, W. A. Bickmore, Mammalian PRP4 kinase copurifies and interacts with components of both the U5 snRNP and the N-CoR deacetylase complexes. *Mol Cell Biol.* **22**, 5141-5156 (2002).
24. E. A. Greene, C. A. Codomo, N. E. Taylor, J. G. Henikoff, B. J. Till, S. H. Reynolds, L. C. Enns, C. Burtner, J. E. Johnson, A. R. Odden, L. Comai, S. Henikoff. Spectrum of chemically induced mutations from a large-scale reverse-genetic screen in Arabidopsis. *Genetics* **164**, 731–740 (2003).
25. A. D. Tang, C. M. Soulette, M. J. van Baren, K. Hart, E. Hrabeta-Robinson, C. J. Wu, A. N. Brooks, Full-length transcript characterization of SF3B1 mutation in chronic lymphocytic leukemia reveals downregulation of retained introns. *Nat Commun*. **11**, 1438 (2020).
26. F. C. Oesterreich, L. Herzel, K. Straube, K. Hujer, J. Howard, K. M. Neugebauer, Splicing of nascent RNA coincides with intron exit from RNA polymerase II. *Cell*, **165**, 372–381 (2016).
27. L. Herzel, K. Straube, K. M. Neugebauer, Long-read sequencing of nascent RNA reveals coupling among RNA processing events. *Genome Res.,* **28**, 1008–1019 (2018).
28. J. Jumper, R. Evans, A. Pritzel, T. Green, M. Figurnov, O. Ronneberger, K. Tunyasuvunakool, R. Bates, A. Žídek, A. Potapenko, A. Bridgland, C. Meyer, S. A. A. Kohl, A. J. Ballard, A. Cowie, B. Romera-Paredes, S. Nikolov, R. Jain, J. Adler, T. Back, S. Petersen, D. Reiman, E. Clancy, M. Zielinski, M. Steinegger, M. Pacholska, T. Berghammer, S. Bodenstein, D. Silver, O. Vinyals, A. W. Senior, K. Kavukcuoglu, P. Kohli, D. Hassabis, Highly accurate protein structure prediction with AlphaFold. *Nature*. **596**, 583-589 (2021).
29. M. Mirdita, S. Ovchinnikov, M. Steinegger, ColabFold - Making protein folding accessible to all. https://www.biorxiv.org/content/10.1101/2021.08.15.456425v1 (2021).
30. S. C. Artim, J. M. Mendrola, M. A. Lemmon, Assessing the range of kinase autoinhibition mechanisms in the insulin receptor family. *Biochem J.* **448**, 213-220 (2012).

31. J. M. Mendrola, F. Shi, J. H. Park, M. A. Lemmon, Receptor tyrosine kinases with intracellular pseudokinase domains. *Biochem Soc Trans*. **41**, 1029-1036 (2013).
32. C. H. Yun, T. J. Boggon, Y. Li, M. S. Woo, H. Greulich, M. Meyerson, M. J. Eck, Structures of lung cancer-derived EGFR mutants and inhibitor complexes: mechanism of activation and insights into differential inhibitor sensitivity. *Cancer Cell.* **11**, 217-27 (2007).
33. T. Nakaoku, T. Kohno, M. Araki, S. Niho, R. Chauhan, P. P. Knowles, K. Tsuchihara, S. Matsumoto, Y. Shimada, S. Mimaki, G. Ishii, H. Ichikawa, S. Nagatoishi, K. Tsumoto, Y. Okuno, K. Yoh, N. Q. McDonald, K. A. Goto, A secondary RET mutation in the activation loop conferring resistance to vandetanib. *Nat Commun*. **9**, 625 (2018).
34. M. Hoemberger, W. Pitsawong, D. Kern, Cumulative mechanism of several major imatinib-resistant mutations in Abl kinase. *Proc Natl Acad Sci U S A*. **117**, 19221-19227 (2020).
35. W. Trager, J. B. Jensen, Human malaria parasites in continuous culture. *Science* **193**, 673–675 (1976).
36. D. C. Farhat, C. Swale, C. Dard, D. Cannella, P. Ortet, M. Barakat, F. Sindikubwabo, L. Belmudes, P. J. De Bock, Y. Couté, A. Bougdour, M. A. Hakimi, A MORC-driven transcriptional switch controls Toxoplasma developmental trajectories and sexual commitment. *Nat Microbiol.* **5**, 570-583 (2020).
37. D. C. Farhat, M. W. Bowler, G. Communie, D. Pontier, L. Belmudes, C. Mas, C. Corrao, Y. Couté, A. Bougdour, T. Lagrange, M. A. Hakimi, C. Swale, A plant-like mechanism coupling m6A reading to polyadenylation safeguards transcriptome integrity and developmental gene partitioning in Toxoplasma. *Elife*. **10**, e68312 (2021).

Acknowledgments. This work was supported by the Laboratoire d'Excellence (LabEx) ParaFrap [ANR-11-LABX-0024], the Agence Nationale pour la Recherche [Project HostQuest, ANR-18-CE15-0023, Project ApiNewDrug, ANR-21-CE35-0010-01, Project EpiKillMal, ANR-20-CE18-0006], the European Research Council [ERC Consolidator Grant N°614880 Hosting TOXO to M.A.H], and Fondation pour la Recherche Médicale [FRM Equipe # EQU202103012571] and Roux-Cantarini Fellowship attributed to FN. The proteomic experiments were partially supported by Agence Nationale de la Recherche under projects ProFI (Proteomics French Infrastructure, ANR-10-INBS-08) and GRAL, a program from the Chemistry Biology Health (CBH) Graduate School of University Grenoble Alpes (ANR-17-

EURE-0003). The HTX Lab (EMBL Grenoble) are thanked for support in screening for crystal conditions and automatic mounting of crystals. **Author Contributions.** M.-A.H. led the research and coordinated the collaboration. M.-A.H. A.B. and C.S. designed the project. Y.C. and L.B. performed the mass spectrometric analyzes. F.L. designed and performed experiments on Eimeria and Cryptosporidium. A.S. and F.N. designed and performed experiments on Plasmodium falciparum. A.B. computed and analyzed the RNA-seq data. V.B. performed the drug screening. V.B. and D. C. performed the in vitro studies with T. gondii. M.-P.B.-P. and V.B. designed and performed the in vivo experiments with T. gondii. C.S. and MWB performed structural studies. C.S. and C.M. performed the MST and SEC-MALLS. C.S. performed nanopore DRS and analyzed them. V.B. and C.S. designed and performed biochemical studies. M.-A.H., A.B., and C.S. interpreted the experimental work and wrote the paper with editorial support from V.B. and fruitful comments from all other authors. **Data availability.** All data associated with this study are in the paper or the Supplementary Materials. All unique and stable reagents generated in this study are available by contacting M.A.H. and completion of a materials transfer agreement. The Nanopore RNAseq data have been deposited in NCBI's SRA data PRJNA774463. The Illumina RNA-seq dataset generated during this study is available at NCBI GEO: GSE193614. The coordinates and structure factors for the *Tg*PRP4k/altiratinib structure have been deposited in the PDB with the accession number 7Q4A. The mass spectrometry proteomics data were deposited with the ProteomeXchange Consortium via the PRIDE partner repository with the record identifier : pxd029455. **Declaration of Interests.** The authors declare no competing interests.

Figures caption.

Fig. 1. Efficacy of altiratinib against the parasite *Toxoplasma gondii*. (**A**) Graphical representation of data from the medium-throughput screen. A cutoff was set at 70% of parasite inhibition. Red dots, hits. The workflow used for the screening is shown in **Fig. S1A**. (**B**) The half-maximal effective concentration (EC_{50}) values of the 14 molecules validated at 1µM. Data are presented as mean ± standard deviation (SD) of n=3 technical replicates. Error bars correspond to 95% confidence intervals. (**C**) Chemical structure of altiratinib. (**D**) EC_{50} values for pyrimethamine and altiratinib. The confluent HFF monolayer was infected with tachyzoites of the *T. gondii* RH_NanoLucEmGFP strain (Table S5). The EC_{50} values of each biological replicate were determined by non-linear regression analysis. EC_{50} data are presented as mean

G SD from 3 independent biological replicates, each with 3 technical replicates. (**E**) Compound efficiency presented by IFA. Confluent HFFs were infected with *T. gondii* RH_NanoLucEmGFP and incubated with 1µM of pyrimethamine, 300 nM of altiratinib or 0.1% of the vehicle (DMSO) for 24h. Fixed cells were stained with anti-inner membrane complex protein (GAP45) antibody (magenta). In green the cytosolic GFP. Scale bar corresponds to 5µm. (**F**) Dose-response curves of HFFs, ARPE-19, MCF7, MDA231 and U937 cell lines in the presence of altiratinib. Human cells were plated out and incubated with increasing concentrations of the drug. After 72h, cell viability was determined using the "*CellTiter-Blue Assay"* kit (Promega) and cell cytotoxicity concentration (CC50) was calculated. The graph is representative of two different experiments performed in triplicate. The shaded error envelopes indicate 95% confidence intervals. On the right, CC50 values show the mean of two experiments. Selectivity index (SI) is based on the average of human CC50 divided by the average of *T. gondii* EC50. (**G**) Effect concentration curve of *Eimeria tenella* in presence of altiratinib. (**H**) Altiratinib inhibition of *Neospora caninum* proliferation shown by plaque assay. After 7 days of infection and drugs incubation, the size of at least 50 plaques were measured. n.d., not detected. (**I**) Dose-response curves of altiratinib and dihydroartemisinin (DHA) in *P. falciparum* asexual blood-stage. Graph is representing the mean and SD values obtained in three independent experiments run in triplicate.

Fig. 2. Deconvolution and validation of the *Tg*PRP4K molecular target. (**A**) Circos plot summarizing the single nucleotide variants (SNVs) detected by transcriptomic analysis of *T. gondii* altiratinib-resistant lines, grouped by chromosome (numbered in Roman numerals with size intervals indicated on the outside). Each dot in the six innermost gray tracks corresponds to a scatter plot of the mutations identified in the six drug-resistant strains, with each ring representing one of the six drug-resistant lines (A through F). Each bar in the outermost track represents the positions of selected archetypal essential genes. See Table S2 for transcriptomic analysis. (**B**) Schematic representation of the *Tg*PRP4K protein structure. The kinase domain is predicted in the C-terminal portion of the protein. Phosphorylated and acetylated residues are shown as blue and red dots, respectively. The orange dots correspond to the three discovered SNVs located in the kinase domain. (**C**) The nuclear location of *Tg*PRP4K (red) in human primary fibroblasts (HFFs) infected with parasites expressing an HA–Flag-tagged copy of *Tg*PRP4K. Cells were co-stained with Hoechst DNA-specific dye (blue) and the anti-Inner Membrane Complex (IMC) (green) antibody. Scale bar, 5 µm. (**D**) Graphs representing the essentiality of *Tg*PRP4K protein assessed by plaque assay. RH_Tir1-Ty and *Tg*PRP4K KD

parasites were either untreated or treated with IAA for 7 days and the size of 42 plaques were measured upon detection. n.d., not detected. (**E**) Fluorescence microscopy showing intracellular growth of WT and the *Tg*PRP4K edited parasites (F647S, L686F, L715F). HFF cells were infected with tachyzoites of the indicated *T. gondii* strains expressing the NLuc-P2A-EmGFP reporter gene and incubated with 300 nM of altiratinib or 0.1% DMSO as control. Cells were fixed 24 h post-infection and then stained with antibodies against the *T. gondii* inner membrane complex protein GAP45 (magenta). The cytosolic GFP is shown in green. Scale bars represent 5 µm. (**F**) EC_{50} values for pyrimethamine (Pyr) and altiratinib were determined for WT and the engineered *Tg*PRP4K mutant strains (F647S, L686F, L715F). The EC50 values on the upper part of the graphs represent the mean ± SD of three biological replicates. On the top of each panel, lines shown the fold change in EC_{50} relative to that of the WT parasites. Dose-response curves are shown in Fig. S6C. (**G**) Effects of *Tg*PRP4K mutations on *T. gondii* lytic cycle as determined by plaque assay. Plaque sizes (n = 50 per condition) were measured for WT and the engineered *Tg*PRP4K mutant strains (F647S, L686F, L715F) after 7 days of growth in the absence or presence of 300 nM of altiratinib. n.d., not detected. Significance was assessed by Mann-Whitney or Kruskal-Wallis tests (One-way ANOVA).

Fig. 3. Structure of the complex *Tg*PRP4K-altiratinib and mechanism of action. (**A**) Thermal stability profile of WT (upper panel) and L715F (bottom panel) recombinant proteins. Each protein was incubated for 3 minutes at different temperatures (from 30° to 69° C) in presence or absence of Altiratinib (100 µM) to quantify the melting temperatures using non-linear regression analysis of normalized data and assuming a sigmoidal dose response. (**B**) Protein–Ligand interaction. WT and L715F recombinant proteins labelled to His-fluorescent dye (100 nM), were incubated with altiratinib from 0.15 nM to 5000 nM. Changes in thermophoresis were plotted as mean changes in Fnorm values against ligand concentration, yielding a Kd of 64 ± 20 nM for WT (upper panel) and 26 ± 2 nM for L715F (bottom panel). Curve 95% confidence intervals are displayed; n= 3. (**C**) Full structure of *Tg*PRP4K (L715F) bound to altiratinib (pdb id: 7Q4A). PRP4K is represented in a cartoon fashion with a transparent surface background with alpha helices colored in orange and beta strands colored in yellow. The activation loop is highlighted in blue, the DFG backbone is shown in pink, the phosphor-serine 729 side chain and altiratinib are shown in a stick representation and colored in grey and cyan respectively. (**D**) Altiratinib binding within *Tg*PRP4K. Zoomed in focus on altiratinib and the key interacting side chains of *Tg*PRP4K shown as grey sticks. Cartoon colors

are the same as used in panel a. (**E**) Sequence alignment of altiratinib *Tg*PRP4K binding regions compared against *Plasmodium falciparum* (*Pf*), *Chromera Velia* (cc), *Schizosaccharomyces pombe* (*Sp*), *Arabidopsis thaliana* (*At*) and *Homo sapiens* (*Hs*) PRP4K/CLK3 orthologs. Key regions are highlighted by pink rectangles, altiratinib interacting amino acids from *Tg*PRP4K are shown by cyan circles while divergent residues in the human ortholog are shown by red triangles. Mutations found in the mutagenesis experiment are highlighted by a green star. The alignment was generated with CLC sequence viewer 7.

Fig. 4. Hinge region selectivity towards altiratinib. (**A**) Hinge region species selectivity towards altiratinib. Cartoon diagram of structurally superposed *Tg*PRP4K (tan) and human PRPF4B (sky blue) with altiratinib in cyan. Hinge region residues are detailed by including stick representations of their side chains. (**B**) Sanger chromatogram validating the *TgPRP4K* gene editing for W649P mutation. On the top, nucleotide positions relative to the ATG start codon on genomic DNA are indicated. (**C**) IFA showing the W649P resistance to altiratinib. Confluent HFFs were infected with engineered parasites and incubated with pyrimethamine (1 µM) or altiratinib (300 nM) for 24h. Fixed cells were stained using anti-GAP45 antibody (magenta) while the cytosolic GFP is showed in green. Scale bar represents 5 µm. (**D**) Graph representing the EC_{50} of W649P for pyrimethamine and altiratinib. Values showed in the upper part on the graph are the mean ± SD of three independent experiment. On the top of the panel, the line shows the fold change in altiratinib EC_{50} relative to pyrimethamine. (**E**) Plaque assay representing the lytic cycle of RH WT and W649P parasites in presence or absence of 300 nM of altiratinib. After 7days of drugs incubation, infected cells were fixed and stained to visualize the presence of lysis plaques (on the left). The area of 50 plaques was measured and represented in the right panel. (**F**) Thermal stability profile of W649P recombinant protein in presence or absence of Altiratinib (100 µM). (**G**) Protein-ligand interaction profile of W649P protein in presence of Altiratinib as measured by thermophoresis with the same assay used in Fig. 3b. Changes in thermophoresis of the mean of three replicates were plotted. Curve 95% confidence intervals are displayed as dotted lines. NA, not available. (**H**) Table showing the melting temperature (Tm) of WT, L715F and W649P recombinant proteins during their incubation with DMSO or Altiratinib (100 µM) at different temperatures. Low interaction between W649P and the compound was detected as showed by the ΔTm values. (**I**) Kinase activity inhibition *in vitro*. KinaseGlo® remaining ATP levels were measured and normalized for every condition.

The normalized endpoint activity is plotted against altiratinib concentrations. 4-parameter inhibition curves were used to determine an apparent IC50 for WT, L715F and W649P mutant.

Fig. 5. Nanopore DRS analysis of altiratinib-induced splicing defects in *T. gondii*. (**A**) General transcriptomic effects of altiratinib treatment. *k*-means clustering of 2400 transcripts treated with EdgeR: log2(CPM+4). The color key ranges from -3 to 3 (green to red), 3 clusters were defined. In each, *Tg*PRP4K WT/L715F/W649P duplicate sequencing experiments are shown in the presence (300 nM) or absence of altiratinib. (**B**) M-pileup representation of the aligned nanopore reads at the *TGME49_214940* loci. WT/L715F/W649P sequencing experiments are shown as grayscale histograms in the presence (300 nM) or absence of altiratinib. (**C** and **D**)**,** FLAIR analysis of *TGME49_211420* (**C**) and TGME49_214940 (**D**) loci. Standard annotation and FLAIR collapsed isoforms (FCI) are shown schematically under a sample view of 15 reads per condition (same conditions as in **B**). Sense and antisense reads are colored red and blue, respectively. Below the FCI representation is an isoform quantification histogram showing duplicate measurements in each WT/L715F/W649P condition and in the presence (300 nM) or absence of altiratinib. The color code is the same as for the above FCI, grey histograms represent minor isoforms which not shown schematically. (**E**) Overall quantification of intron retention. Scatter plot of intron retention ratios (per averaged duplicate transcript) are shown for *T. gondii* and *H. sapiens*. WT/L715F/W649P strains that were untreated (in green) or treated (300 nM, in cyan) are shown, the black histogram shows the median, the whiskers show the interquartile range. Significance between the WT untreated and treated conditions was calculated using a non-parametric Friedman test.

Fig. 6. Cross-species selectivity of altiratinib analysed by nanopore DRS. (**A**) Splicing defects induced by altiratinib in *P. falciparum*. M-pileup representation of aligned nanopore reads at the *PF3D7_0918100* and *PF3D7_1118700* loci. Untreated (UT) or altiratinib-treated (2.5 µM) sequencing experiments are shown as grayscale histograms. Shown below are IGB samples from 10 individual aligned reads using sense (purple) and antisense (blue) coloring under UT and treated conditions. (**B**) Overall quantification of intron retention in *P. falciparum*. Scatter plots of intron retention ratios (per averaged duplicate transcript) are shown for untreated (in green) or altiratinib treated (in cyan) conditions, the black histogram shows the median, the whiskers show the interquartile range. Significance between the WT untreated and treated conditions was calculated using a nonparametric Mann-Whitney *t*-test. (**C**) Splicing consistency is maintained in *C. parvum*. M-pileup and IGB sampling of aligned reads from

untreated (UT) or altiratinib treated (0.5 μM) *C. parvum* at the highly transcribed and spliced *cdg6_4620* loci. (**D**) Overall quantification of intron retention in *C. parvum*. The same display rules as in **B**. were applied. (**E**) Thermal shift assay of TgPRP4K and PfCLK3 in the presence of altiratinib (100 μM) or TCDM-135051 (100 μM). A simplicate assay is shown, but the measurement was replicated. (**F**) Hinge region species selectivity towards TCMD-135051. Cartoon diagram of the structurally superposed *Tg*PRP4K from this work (in tan) and the alphaflod2 predicted *Pf*CLK3 (dodger blue) with TCDM-135051 modelling in orange. The residues of the hinge region are also detailed by showing their side chains as stick representations.

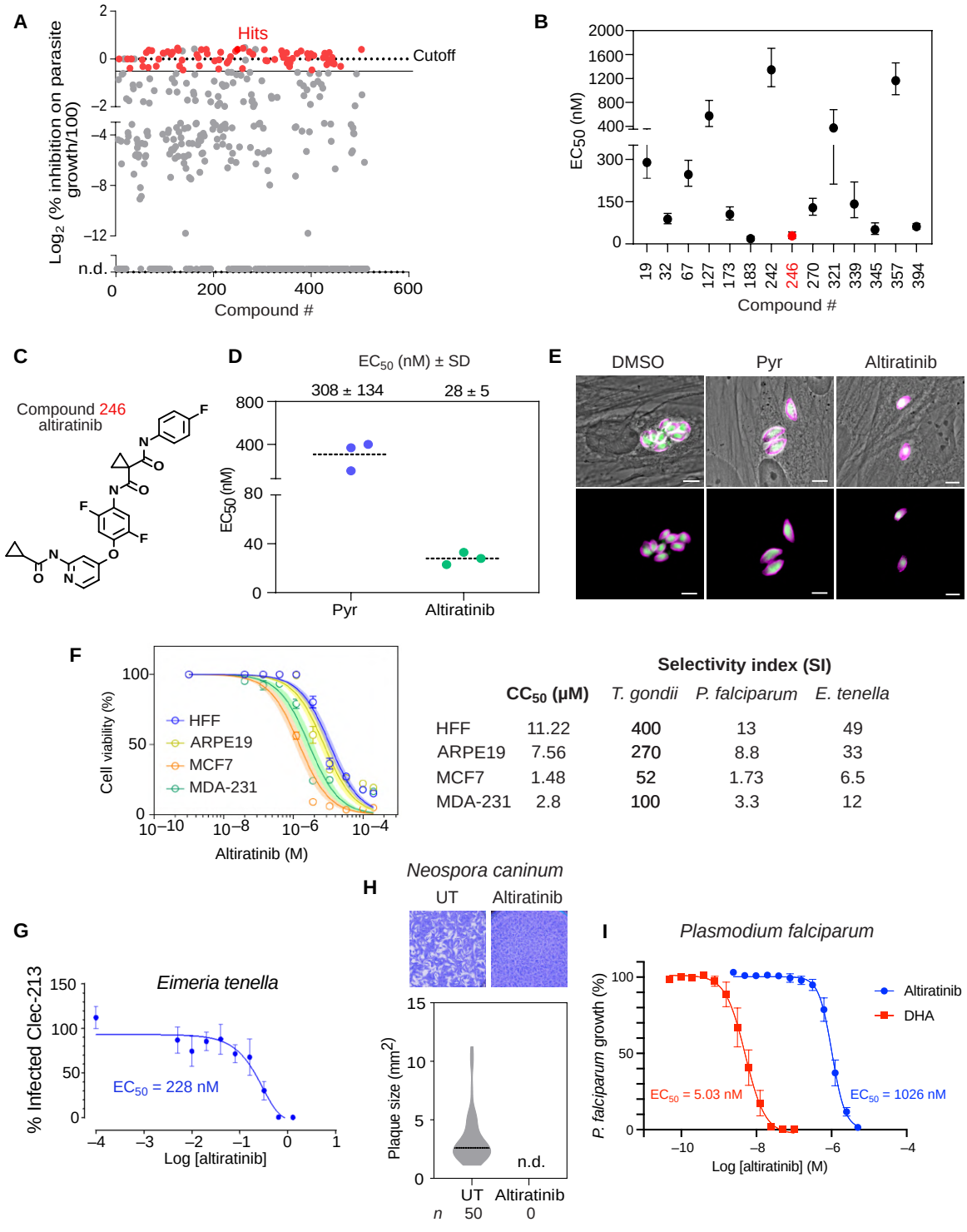
A
Hits
Cutoff
Log2 (% inhibition on parasite growth/100)
n.d.
Compound #
B
EC50 (nM)
Compound #
C
Compound 246
altiratinib
D
EC50 (nM) ± SD
308 ± 134
28 ± 5
EC50 (nM)
Pyr
Altiratinib
E
DMSO
Pyr
Altiratinib
F
Cell viability (%)
HFF
ARPE19
MCF7
MDA-231
Altiratinib (M)
Selectivity index (SI)
CC50 (µM)
T. gondii
P. falciparum
E. tenella
HFF 11.22 400 13 49
ARPE19 7.56 270 8.8 33
MCF7 1.48 52 1.73 6.5
MDA-231 2.8 100 3.3 12
G
Eimeria tenella
% Infected Clec-213
EC50 = 228 nM
Log [altiratinib]
H
Neospora caninum
UT
Altiratinib
Plaque size (mm2)
n.d.
n
50
0
I
Plasmodium falciparum
P. falciparum growth (%)
Altiratinib
DHA
EC50 = 5.03 nM
EC50 = 1026 nM
Log [altiratinib] (M)

Figure 1

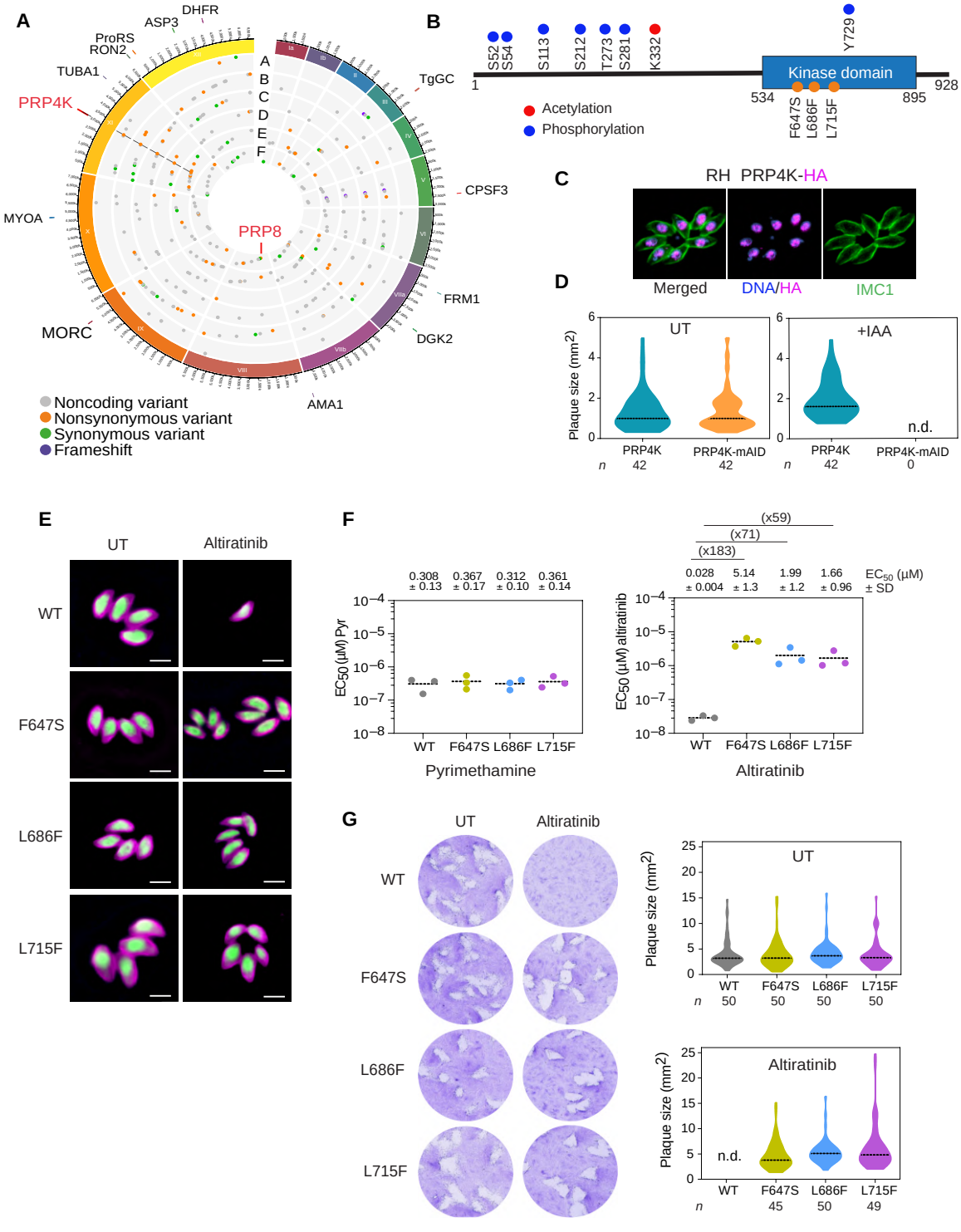
A
DHFR
ASP3
ProRS
RON2
TUBA1
PRP4K
TgGC
CPSF3
MYOA
PRP8
FRM1
MORC
DGK2
AMA1
A
B
C
D
E
F
Noncoding variant
Nonsynonymous variant
Synonymous variant
Frameshift
B
S52
S54
S113
S212
T273
S281
K332
Y729
Kinase domain
1
534
895
928
F647S
L686F
L715F
Acetylation
Phosphorylation
C
RH PRP4K-HA
Merged
DNA/HA
IMC1
D
UT
+IAA
Plaque size (mm2)
PRP4K
PRP4K-mAID
n
42
42
42
0
n.d.
E
UT
Altiratinib
WT
F647S
L686F
L715F
F
(x59)
(x71)
(x183)
0.308 ± 0.13
0.367 ± 0.17
0.312 ± 0.10
0.361 ± 0.14
0.028 ± 0.004
5.14 ± 1.3
1.99 ± 1.2
1.66 ± 0.96
EC50 (μM) ± SD
EC50 (μM) Pyr
EC50 (μM) altiratinib
WT F647S L686F L715F
Pyrimethamine
Altiratinib
G
UT
Altiratinib
WT
F647S
L686F
L715F
Plaque size (mm2)
WT F647S L686F L715F
n 50 50 50 50
n.d.
n 45 50 49

Figure 2

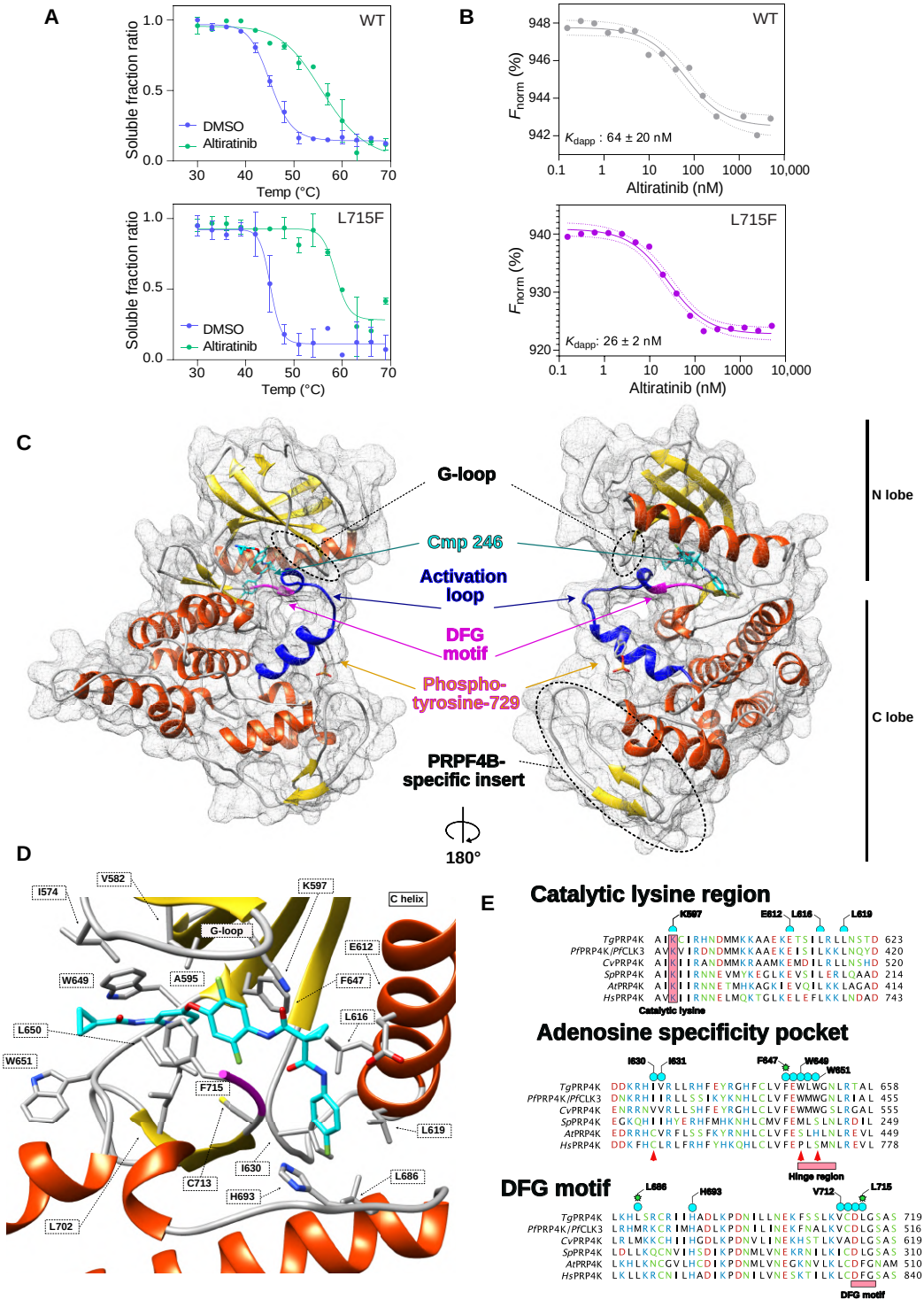
A
WT
Soluble fraction ratio
DMSO
Altiratinib
Temp (°C)
L715F
B
WT
F_{norm} (%)
K_{dapp} : 64 ± 20 nM
Altiratinib (nM)
L715F
K_{dapp}: 26 ± 2 nM
C
G-loop
Cmp 246
Activation loop
DFG motif
Phospho-tyrosine-729
PRPF4B-specific insert
180°
N lobe
C lobe
D
V582
I574
K597
C helix
G-loop
E612
W649
A595
F647
L650
L616
W651
F715
L619
I630
C713
L686
H693
L702
E
Catalytic lysine region
K597
E612
L616
L619
TgPRP4K
PfPRP4K/PfCLK3
CvPRP4K
SpPRP4K
AtPRP4K
HsPRP4K
Catalytic lysine
Adenosine specificity pocket
I630
I631
F647
W649
W651
Hinge region
DFG motif
L686
H693
V712
L715
DFG motif

Figure 3

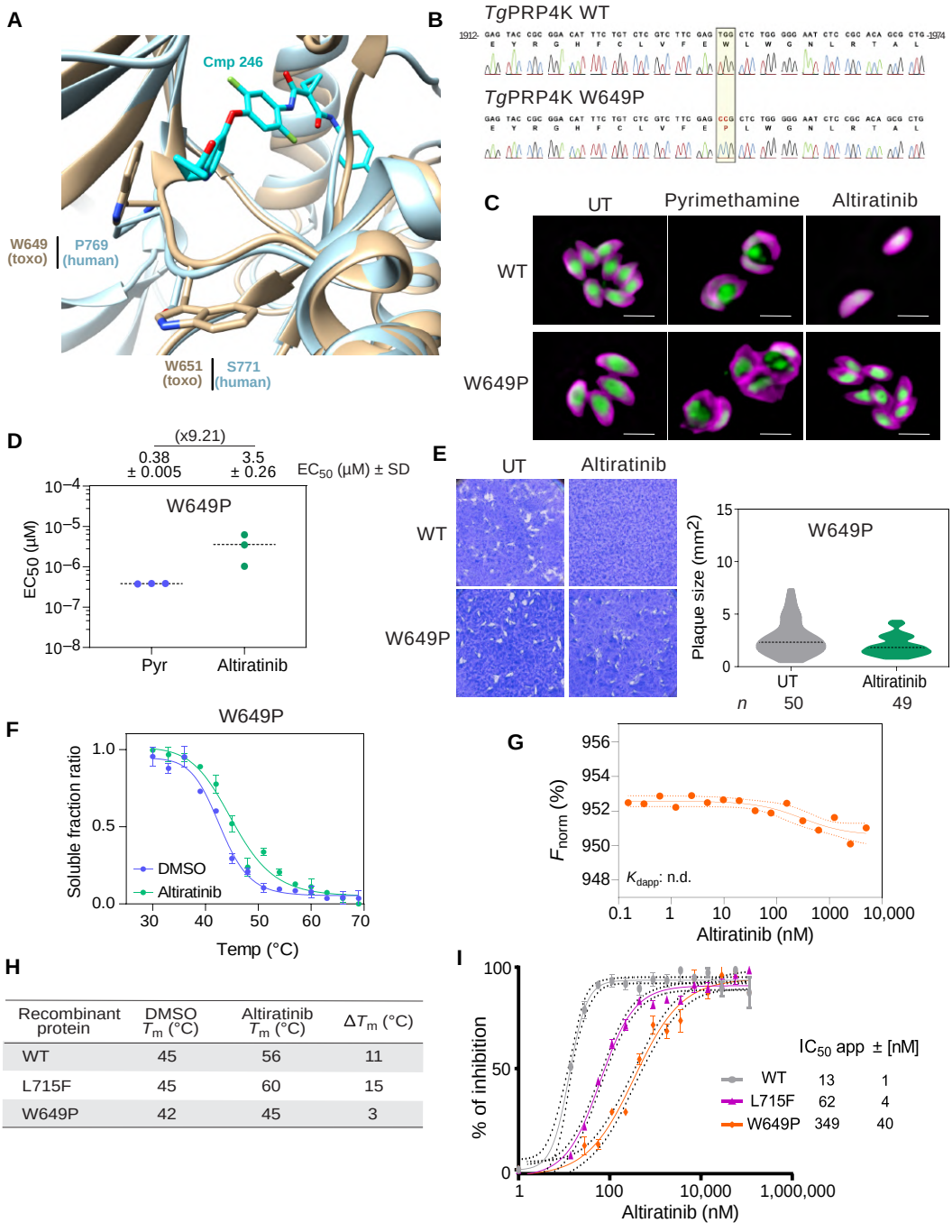

Recombinant protein	DMSO T_m (°C)	Altiratinib T_m (°C)	ΔT_m (°C)
WT	45	56	11
L715F	45	60	15
W649P	42	45	3

Figure 4

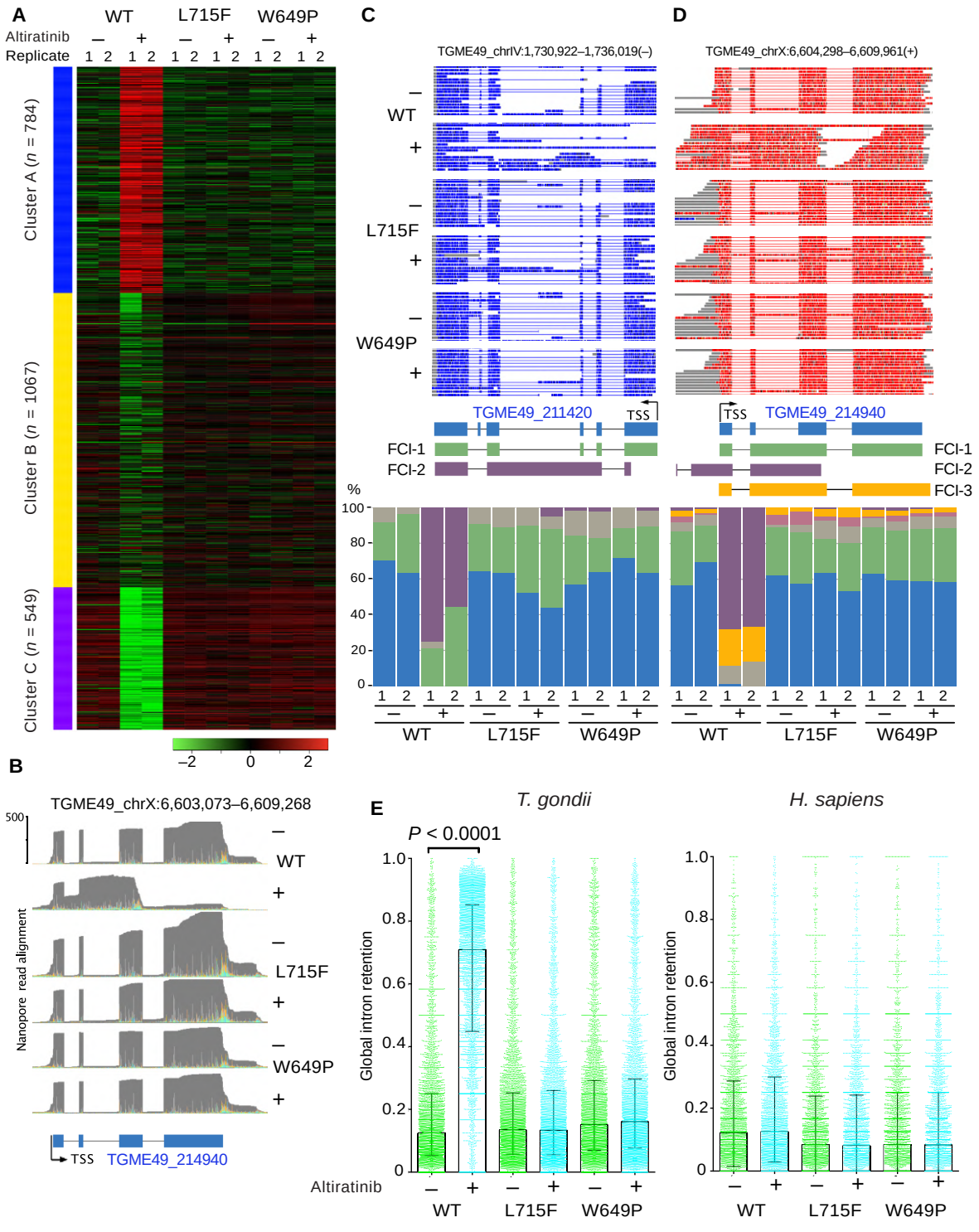
A
WT
L715F
W649P
Altiratinib
Replicate
Cluster A (n = 784)
Cluster B (n = 1067)
Cluster C (n = 549)
B
TGME49_chrX:6,603,073–6,609,268
Nanopore read alignment
TSS
TGME49_214940
C
TGME49_chrIV:1,730,922–1,736,019(–)
TGME49_211420
FCI-1
FCI-2
%
D
TGME49_chrX:6,604,298–6,609,961(+)
TGME49_214940
FCI-3
E
T. gondii
H. sapiens
P < 0.0001
Global intron retention
Altiratinib

Figure 5

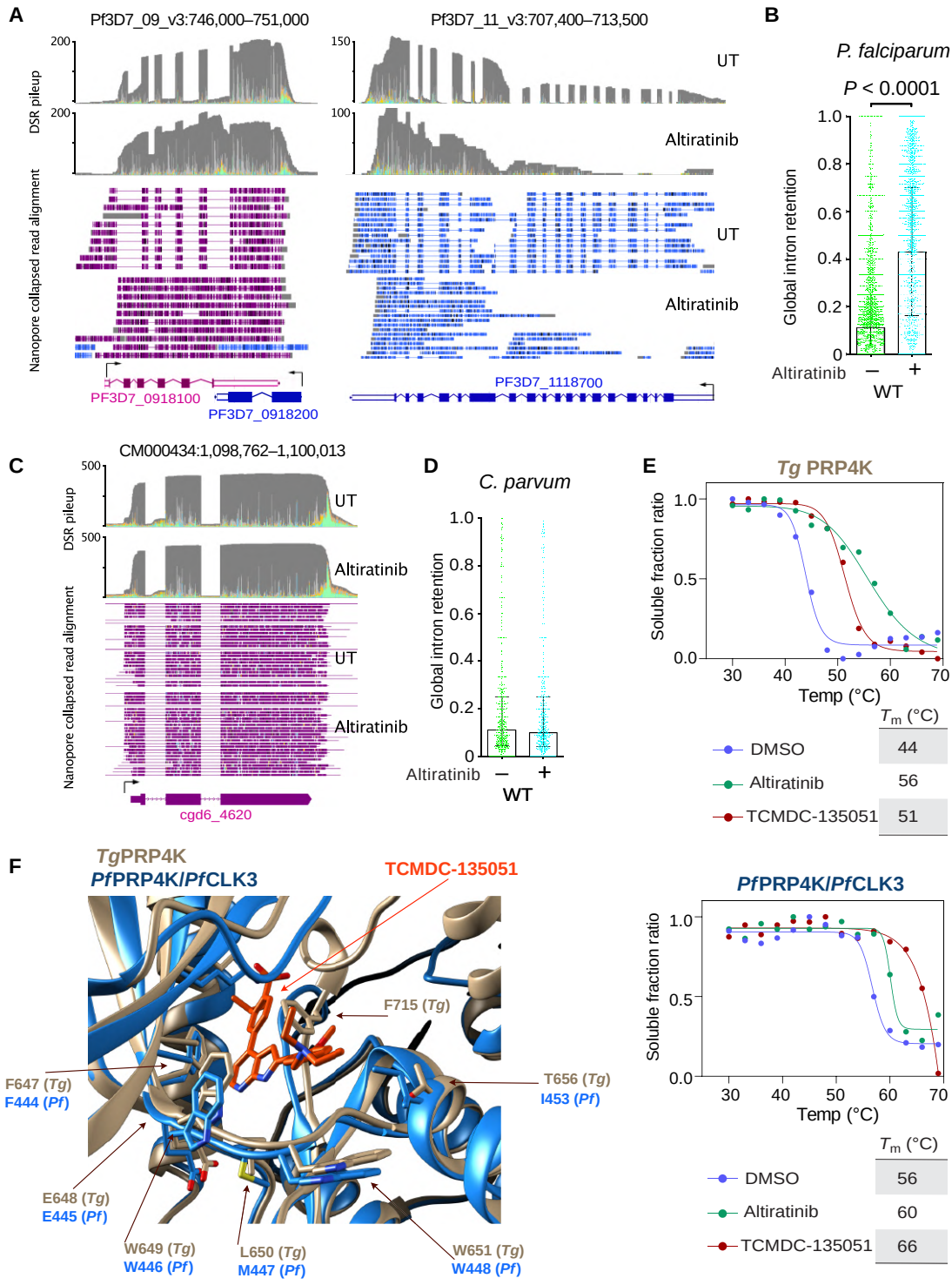
A
Pf3D7_09_v3:746,000–751,000
Pf3D7_11_v3:707,400–713,500
DSR pileup
Nanopore collapsed read alignment
UT
Altiratinib
PF3D7_0918100
PF3D7_0918200
PF3D7_1118700
B
P. falciparum
P < 0.0001
Global intron retention
Altiratinib
WT
C
CM000434:1,098,762–1,100,013
cgd6_4620
D
C. parvum
E
Tg PRP4K
Soluble fraction ratio
Temp (°C)
Tm (°C)
DMSO 44
Altiratinib 56
TCMDC-135051 51
F
TgPRP4K
PfPRP4K/PfCLK3
TCMDC-135051
F715 (Tg)
F647 (Tg)
F444 (Pf)
T656 (Tg)
I453 (Pf)
E648 (Tg)
E445 (Pf)
W649 (Tg)
W446 (Pf)
L650 (Tg)
M447 (Pf)
W651 (Tg)
W448 (Pf)
DMSO 56
Altiratinib 60
TCMDC-135051 66

Figure 6